Fractographic identification of fracture origin mainly controlled by the intensity of singular stress field (ISSF) in prismatic butt joint with corner fillet

doi: https://doi.org/10.1016/j.ijadhadh.2021.102810

Fractographic Identification of Fracture Origin Mainly Controlled by the Intensity of Singular Stress Field (ISSF) in Prismatic Butt Joint with Corner Fillet

Rei Takaki[1], Nao-Aki Noda[1*], Yoshikazu Sano[1],
Yasushi Takase[1], Yasuaki Suzuki[2], Ching-Kong Chao[3]

[1]*Department of Mechanical Engineering, Kyushu Institute of Technology, 1-1 Sensui-cho,Tobata-ku,Kitakyushu-shi,Fukuoka 804-8550, Japan*

[2]*Suzuki Adhesion Institute of Technology, 131 Aza-yashiki, Ukino, Chiaki-cho, Ichinomiya-shi, Aichi 491-0806 Japan*

[3]*Department of Mechanical Engineering, National Taiwan University of Science and Technology, No.43 Keelung Road Sec.4 Da'an-Dist, Taipai-City, 10607, Taiwan*

ABSTRACT

In this study, the fracture origin is identified for the prismatic butt joints whose debonding condition can be expressed as a constant value of the ISSF. The ISSF variation is newly analyzed along the interface side by considering the real specimen geometry with chamfer at the corner. The detail fractographic observation shows that most of the fracture starts from the maximum ISSF region at the interface side instead of the interface corner. When the bondline thickness *h* is larger, the fracture origin can be seen at sub-surface because the stress triaxiality decreases inside of the specimen. The fracture origin under thermal loading can be estimated similarly because of the coincidence the ISSF variations.

Keywords

Adhesion, Debonding strength, Prismatic butt joint, Intensity of singular stress (ISSF), Fracture origin, Fracture surface, Fillet

*Corresponding Author: Nao-Aki Noda. Email: naoaki.noda844@mail.kyutech.jp

Nomenclature

E	Young's modulus	α, β	Dundurs parameter
F_{σ}^{Side}	Dimensionless ISSF	λ	Singular index
$F_{\sigma\ max}^{Side}$	Maximum dimensionless ISSF	υ_j	Poisson's ratio
$F_{\sigma\ min}^{Side}$	Minimum dimensionless ISSF	ρ	Fillet radius
F_{σ}^{REF}	Dimensionless ISSF for reference problem	σ_c	Remote debonding strength
G_j	Shear modulus	σ_z^{∞}	Remote tensile strength
h	Adhesive bondline thickness	$\sigma_{z\ FEM}^{Side}$	FEM stress for 3D model
K_{σ}^{Side}	Intensity of singular stress field (ISSF)	$\sigma_{z\ FEM}^{2D}$	FEM stress for 2D model
K_{σ}^{REF}	ISSF for reference problem	$\sigma_{z\ Real}^{Side}$	True stress
W	Specimen width	$\sigma_{z\ FEM}^{REF}$	FEM stress for reference problem

1. Introduction

Electronic devices are becoming more functional and smaller to satisfy higher performance requirement. Semiconductor packaging technology has to support such smaller structures and faster transmission signals and logic and memory applications. Semiconductor packaging includes a large number of interfaces formed by combining various different materials such as connecting a semiconductor and a substrate, sealing with resin, and forming a semiconductor chip and wiring into a multilayer structure. The stress distribution along the adhesive interface was treated in many papers to ensure the reliability of electronic devices and industrial products [1-8]. This is because the different mechanical properties cause the singular stress field at the interface end [9-16]. Although the bonded strength of the butt joint in Fig. 1 (a) can be expressed as shown in Fig. 1 (b) by the remote tensile stress, it can be expressed as a constant value of the ISSF as shown in Fig.1 (c) (see Appendix A). In our previous papers, by applying 3D modelling as well as 2D modelling, the ISSFs distributions were analyzed along the interface side including the sharp interface corner and also rounded interface corner

[16, 17]. However, the fracture origin controlled by the ISSF was not investigated in detail yet.

In this study, therefore, the detail experimental observation will be performed for the prismatic butt joint specimen in Fig. 1 [18] to identify the fracture origin. The ISSF analysis will be newly applied to the real specimen geometry especially focusing on the largest ISSF region in relation to the fracture origin. Since electric device failures usually occur under thermal loading, the thermal ISSF variation will be also discussed. The interface geometry of prismatic butt joint treated in this paper is fundamental including straight and circular-arc portions. The discussion will be useful for understanding other adhesive joints debonding.

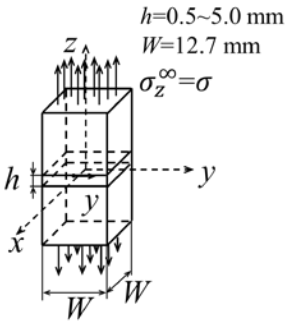

(a) Prismatic butt joint

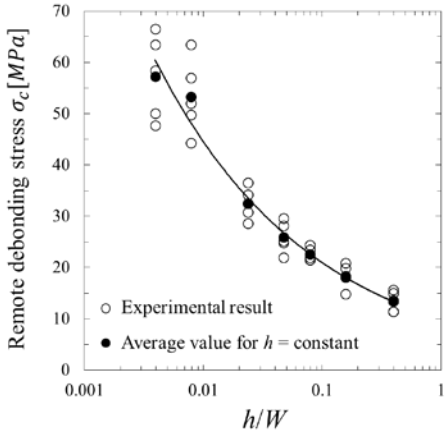

(b) Critical remote tensile stress σ_c

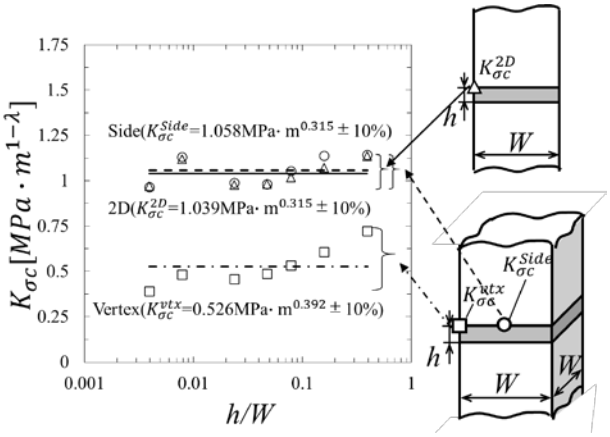

(c) Bonded strength expressed by critical ISSFs

Fig. 1 Prismatic butt joint and bonded strength (see Appendix A)

2. ISSF variation along the interface edge for prismatic butt joint with corner fillet

2.1 Definition of ISSF

In this study, the fracture origin will be identified for Suzuki's specimens [18] by utilizing the ISSF variation newly analyzed. The details of Suzuki's original experimental results as well as the authors' previous ISSF results are indicated in Table A1 in Appendix A. Fig. 2 illustrates the analysis model for the specimen used in the experiment when the corner fillet has the radius ρ=a. The ISSF $K_\sigma^{Side}(y)$ can be defined from the real stress $\sigma_{z\,Real}^{Side}(r,y)$ along the interface side in Fig.1 (a) and the ISSFs $K_\sigma^{Side}(\theta)$ can be defined from the real stress $\sigma_{z\,Real}^{Side}(r,\theta)$ around the corner fillet in Fig. 2 as shown in equation (1).

$$\begin{aligned} K_\sigma^{Side}(y) &= \lim_{r\to 0}\left[r^{1-\lambda}\times\sigma_{z\,Real}^{Side}(r,y)\right] \\ K_\sigma^{Side}(\theta) &= \lim_{r\to a}\left[(a-r)^{1-\lambda}\times\sigma_{z\,Real}^{Side}(r,\theta)\right] \end{aligned} \tag{1}$$

The normalized ISSFs $F_\sigma^{Side}(y)$, $F_\sigma^{Side}(\theta)$ can be expressed by equation (2). Here, σ_z^∞ denotes the remote tensile stress as shown in Fig. 1(a).

$$\begin{aligned} F_\sigma^{Side}(y) &= \frac{K_\sigma^{Side}(y)}{\sigma_z^\infty W^{1-\lambda}} = \frac{\lim_{r\to 0}\left[r^{1-\lambda}\times\sigma_{z\,Real}^{Side}(r,y)\right]}{\sigma_z^\infty W^{1-\lambda}} \\ F_\sigma^{Side}(\theta) &= \frac{K_\sigma^{Side}(\theta)}{\sigma_z^\infty W^{1-\lambda}} = \frac{\lim_{r\to a}\left[(a-r)^{1-\lambda}\times\sigma_{z\,Real}^{Side}(r,\theta)\right]}{\sigma_z^\infty W^{1-\lambda}} \end{aligned} \tag{2}$$

In Eq. (2), $F_\sigma^{Side}(\theta)$ is normalized by $\sigma_z^\infty W^{1-\lambda}$ to be compared with $F_\sigma^{Side}(y)$ [16] at the straight edge. In equations (1) and (2), λ is a singularity index, which can be obtained from the eigen equation (3) [19, 20].

$$\left[\sin^2\left(\frac{\pi}{2}\lambda\right)-\lambda^2\right]^2\beta^2+2\lambda^2\left[\sin^2\left(\frac{\pi}{2}\lambda\right)-\lambda^2\right]^2\alpha\beta+\lambda^2[\lambda^2-1]\alpha^2+\frac{\sin^2(\lambda\pi)}{4}=0 \quad (3)$$

$$\alpha=\frac{G_1(\kappa_2+1)-G_2(\kappa_1+1)}{G_1(\kappa_2+1)+G_2(\kappa_1+1)}, \quad \beta=\frac{G_1(\kappa_2-1)-G_2(\kappa_1-1)}{G_1(\kappa_2+1)+G_2(\kappa_1+1)} \quad (4)$$

$$\kappa_j=\begin{cases}\dfrac{3-\nu_j}{1+\nu_j}\ (\text{plane stress})\\ 3-4\nu_j\ (\text{plane strain})\end{cases}\ (j=1,2) \quad (5)$$

Here, α , β are Dundurs parameters [18,19] defined from Poisson's ratio ν_j and shear modulus G_j of the adherend and adhesive (j = 1 for the adherend, j = 2 for the adhesive) as shown in equations (4) and (5). It is known that when α (α-2β) > 0 the real stress $\sigma_{z\,Real}^{Side}$ has a singularity of the form $\sigma_{z\,Real}^{Side} \propto 1/r^{1-\lambda}$ ($\lambda < 1$) [17, 21]. Table 1 shows the mechanical properties of the adherend and the adhesive used in the experiment with Dundurs parameter α, β and singularity index λ [18-20]. The analysis method is shown in the Appendix [13-16].

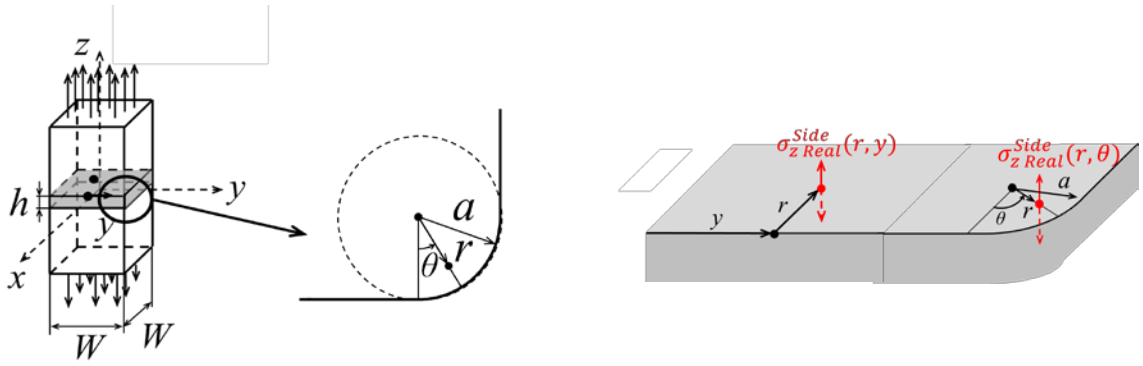

Fig. 2 Prismatic butt joint model with fillet considered in this study

Table 1 Material properties of adhesive and adherend

	Material		Young's modulus E [GPa]	Poisson's ratio ν	α	β	λ
Steel/Resin A	Adherend	S35C	210	0.30	0.969	0.199	0.685
	Adhesive	Epoxy resin A (Brittle)	3.14	0.37			
Steel/Resin B	Adherend	S35C	210	0.30	0.978	0.188	0.674
	Adhesive	Epoxy resin B	2.16	0.38			

		(Ductile)					

2.2 ISSF variation of prismatic butt joint by varying fillet radius at the corner

In the previous studies the proportional method to calculate the ISSF was explained in detail [13-16, 23-25, 29-31]. In this study, therefore, how to obtain the ISSF is briefly described in Appendix B. Then, the fracture origin will be identified on the basis of the ISSF obtained in this study. Fig.3 shows the chamfer at the interface corner of the specimen used in the experiment in Fig.1 (a). If chamfer is modelled by the straight line, two entry corners have the different singular index. Therefore, in this study, to simplify the discussion, the fillet model is applied as shown in Fig. 3 (b) [16, 29]. As shown in Fig. 3, the real chamfering dimension can be modelled by the corner fillet radius ρ= 0.127mm (ρ/W= 0.01). It should be noted that chamfers as shown in Fig. 3 are essential for mechanical components to prevent humans' injuries, and also to prevent damage to other components. Although in Fig.3 the chamfering dimension is smaller, usually the minimum chamfering dimension is about 0.2mm [16, 22]. Therefore, the fillet radius $\rho \geq 0.2$ mm should be investigated as the common chamfering in addition to ρ= 0.127mm. In this study, ISSF variation is discussed by varying the fillet radius ρ to clarify the effect. Table 2 shows the ISSFs in Fig.1 (a) under fixed h =0.127mm (h/W =0.01, W =12.7mm) by varying ρ in the range as ρ=0~6.35mm (ρ/W = 0, 0.0005, 0.001, 0.01, 0.05).

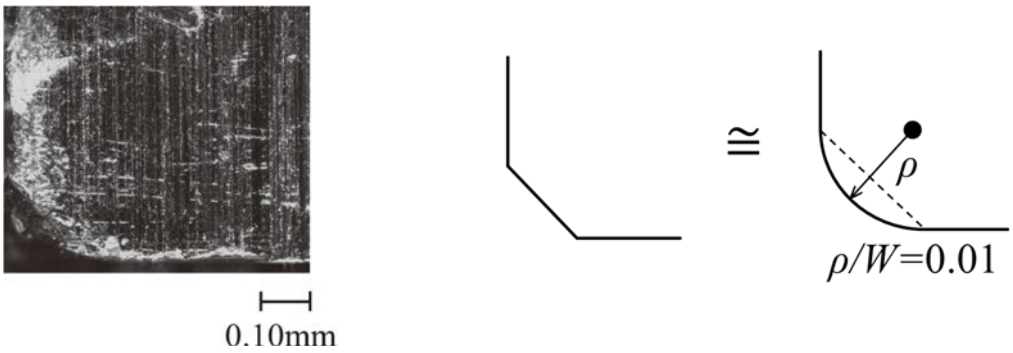

(a) Chamfer at the interface corner of the specimen (b) Chamfered corner modelled by corner fillet of ρ/W= 0.01 (ρ= 0.127mm)

Fig. 3 Enlarged view of the specimen corner

Table 2 $F_{\sigma}^{Side}(y)$ (×10^{-2}) and $F_{\sigma}^{Side}(\theta)$ (×10^{-2}) under fixed h/W =0.01(h =0.127mm, W =12.7mm) by varying fillet radius ρ/W (ρ=0~6.35mm)

(**Bold**: maximum value, *Italic*: minimum values)

(a) Steel/Resin A

y/W or θ	$\rho/W\rightarrow 0$ $\rho\rightarrow$0mm $\rho/h\rightarrow 0$	ρ/W= 0.0005 ρ=0.00635mm ρ/h=0.05	ρ/W= 0.001 ρ=0.0127mm ρ/h=0.1	ρ/W= 0.01 ρ=0.127mm ρ/h=1	ρ/W= 0.05 ρ=0.635mm ρ/h=5	ρ/W=0.5 ρ=6.35mm ρ/h=50
y/W =0	9.09	8.92	9.13	9.00	8.98	9.00
y/W =0.400	9.14	8.95	9.19	9.06	9.02	—
y/W =0.410	9.14	8.96	9.19	9.06	9.02	—
y/W =0.420	9.15	8.96	9.19	9.07	**9.03**	—
y/W =0.430	9.15	8.97	9.20	9.07	9.02	—
y/W =0.440	9.16	8.97	9.21	9.08	9.01	—
y/W =0.450	9.17	8.98	9.21	9.09	8.95	—
y/W =0.460	9.17	8.99	**9.22**	**9.10**	—	—
y/W =0.470	9.16	9.00	9.08	9.07	—	—
y/W =0.480	9.03	8.86	9.12	8.91	—	—
y/W =0.490	8.38	8.20	8.41	8.37	—	—
y/W =0.491	8.24	8.07	8.28	—	—	—
y/W =0.492	8.09	7.92	8.12	—	—	—
y/W =0.493	7.92	7.75	7.95	—	—	—
y/W =0.494	7.72	7.57	7.76	—	—	—
y/W =0.495	7.52	7.37	7.55	—	—	—
y/W =0.496	7.31	7.17	7.34	—	—	—
y/W =0.497	7.12	7.00	7.16	—	—	—
y/W =0.498	*6.97*	*6.91*	*7.04*	—	—	—
y/W =0.499	7.00	7.10	7.67	—	—	—
y/W =0.4995	7.15	7.83	—	—	—	—
y/W =0.500	$\rightarrow\infty$	—	—	—	—	—
θ=0°	—	7.83	7.72	8.37	8.95	9.00
θ=15°	—	8.57	8.41	8.42	8.88	9.00
θ=30°	—	9.03	8.84	8.39	*8.87* (y/W =0.475)	9.00
θ=45°	—	**9.18**	8.99	*8.37* (y/W=0.497)	*8.87* (y/W =0.486)	9.00
θ=60°	—	9.03	8.84	8.39	*8.87* (y/W =0.493)	9.00
θ=75°	—	8.57	8.41	8.42	8.88 (y/W =0.498)	9.00
θ=90°	—	7.83	7.72	8.37	8.95	9.00

(b) Steel/Resin B

y/W or θ	$\rho/W\rightarrow 0$ 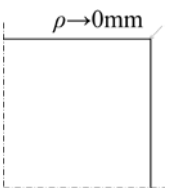 $\rho/h\rightarrow 0$	ρ/W= 0.0005 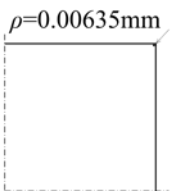 ρ/h=0.05	ρ/W= 0.001 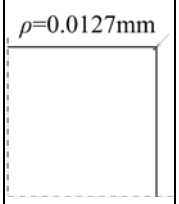 ρ/h=0.1	ρ/W= 0.01 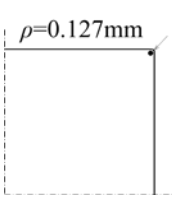 ρ/h=1	ρ/W= 0.05 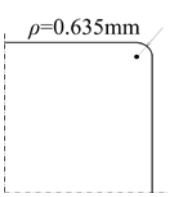 ρ/h=5	ρ/W=0.5 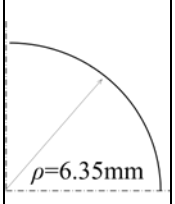 ρ/h=50
y/W =0	8.40	8.06	8.30	8.26	8.3	8.40
y/W =0.400	8.44	8.08	8.35	8.3	8.33	—
y/W =0.410	8.44	8.09	8.35	8.31	8.33	—
y/W =0.420	8.44	8.09	8.36	8.31	**8.33**	—
y/W =0.430	8.44	8.1	8.37	8.32	8.33	—
y/W =0.440	8.44	8.1	8.37	8.33	8.32	—
y/W =0.450	8.44	8.11	8.38	8.33	8.24	—
y/W =0.460	8.42	8.11	**8.38**	**8.33**	—	—
y/W =0.470	8.41	8.09	8.36	8.31	—	—
y/W =0.480	8.21	7.98	8.23	8.14	—	—
y/W =0.490	7.29	7.34	7.58	7.49	—	—
y/W =0.491	7.18	7.22	7.45	—	—	—
y/W =0.492	7.06	7.07	7.30	—	—	—
y/W =0.493	6.95	6.92	7.13	—	—	—
y/W =0.494	6.83	6.74	6.95	—	—	—
y/W =0.495	6.72	6.55	6.76	—	—	—
y/W =0.496	6.66	6.37	6.56	—	—	—
y/W =0.497	6.61	6.20	6.38	—	—	—
y/W =0.498	6.56	*6.12*	*6.27*	—	—	—
y/W =0.499	*6.50*	6.28	6.92	—	—	—
y/W =0.4995	6.58	6.93	—	—	—	—
y/W =0.500	$\rightarrow\infty$	—	—	—	—	—
θ=0°	—	6.92	6.92	7.49	8.24	8.40
θ=15°	—	7.6	7.55	7.51	8.15	8.40
θ=30°	—	8.02	7.95	7.48	*8.13* (y/W =0.475)	8.40
θ=45°	—	**8.16**	8.08	7.47 (y/W =0.497)	*8.13* (y/W =0.486)	8.40
θ=60°	—	8.02	7.95	7.48	*8.13* (y/W =0.493)	8.40
θ=75°	—	7.60	7.55	7.51	8.15	8.40
θ=90°	—	6.92	6.92	7.49	8.24	8.40

Fig. 4 illustrates the ISSF variations along the interface edge for Steel/Resin A. Fig. 4 (b), (d) shows the detail around the interface corner. Fig. 5 illustrate the ISSF variations along the interface edge for Steel/Resin B. From Fig. 4 and Fig. 5, the ISSF variations for Steel/Resin A and Steel/Resin B are nearly the same within 9% error. As shown in Table 2(a) and (b), the maximum ISSF appears at $y/W\cong$ 0.46 in most cases when $\rho/W \geq 0.001$. From W = 12.7 mm and $\rho \geq 0.2$ mm in Fig. 2, $\rho/W \geq 0.016\cong$

0.2/12.7 should be considered as common chamfering. Since $\rho/W \geq 0.016 \geq 0.001$, the maximum ISSF usually appears at $y/W \cong 0.46$ in Fig. 2.

Fig. 4(c)

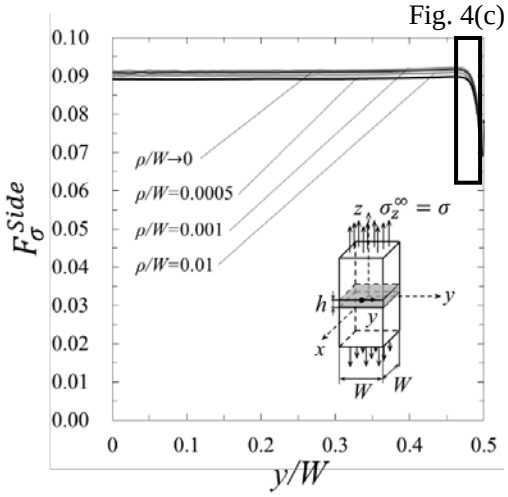

(a) When ρ/W=0~0.01

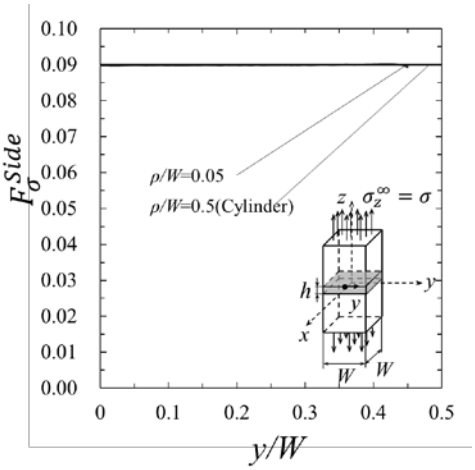

(b)When ρ/W=0.05~0.5

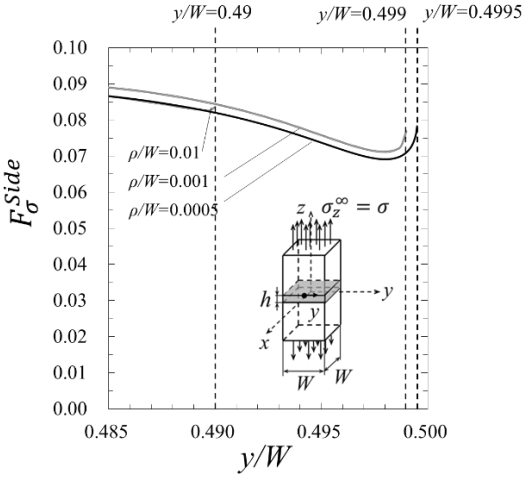

(c) Detail in Fig. 4(a)

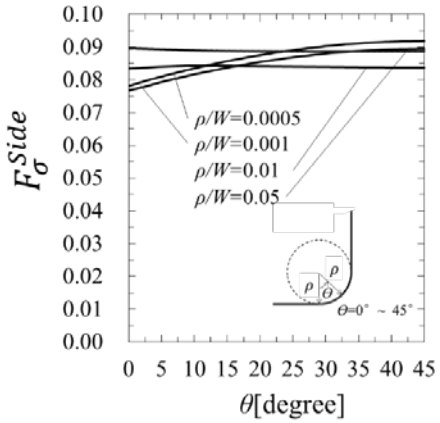

(d) Detail at fillet in Fig. 4(a)

Fig. 4 ISSF distributions on the edge of fillet for Steel/Resin A

Fig. 5(c)

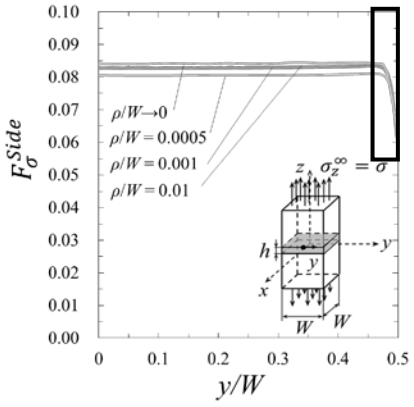

(a) When ρ/W=0~0.01

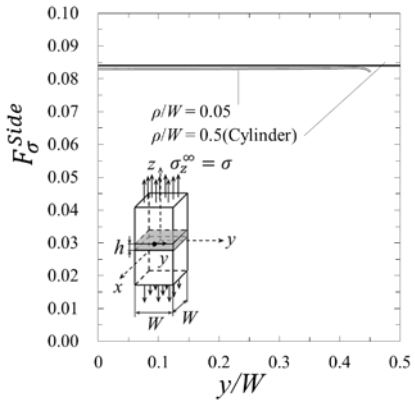

(b)When ρ/W=0.05~0.5

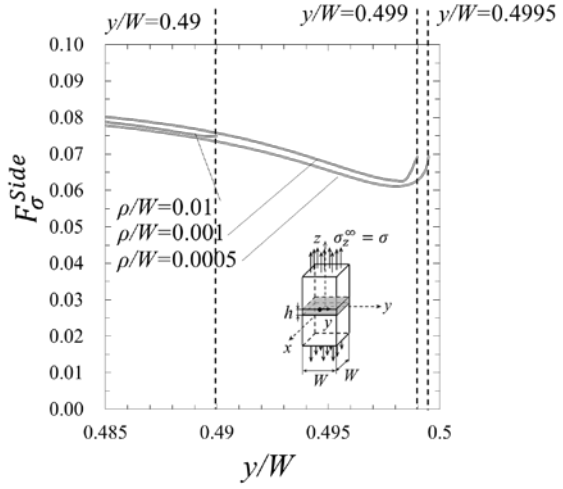

(c) Detail in Fig. 5(a)

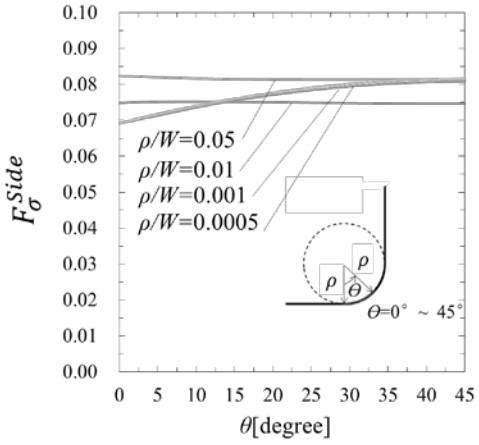

(d) Detail at fillet in Fig. 5(a)

Fig. 5 ISSF distributions on the edge of fillet for Steel/Resin B

Fig. 6 illustrates the maximum ISSF $F_{\sigma\,max}^{Side}$ and the minimum ISSFs $F_{\sigma\,min}^{Side}$ by varying ρ/W. The maximum value $F_{\sigma max}^{Side}$ is insensitive to ρ/W in the range $\rho/W \leq 0.0005$ within 2% variation. The minimum $F_{\sigma min}^{Side}$ is almost constant when $\rho/W \leq 0.001$ and increases with increasing ρ/W when $\rho/W \geq 0.001$. From Fig. 6, it is found that $F_{\sigma\,max}^{Side}$ and $F_{\sigma\,min}^{Side}$ variations for Steel/Resin A and Steel/Resin B are nearly the same within 9% error. It appears that the variation of the ISSF mainly depends on the geometric aspects but shows little sensitivity to the material differences as observed in Figs. 4-6. This is probably a general observation because for metal/resin combinations Dundurs

parameters are in the limited range $0.84 \leq \alpha \leq 1.0,\ 0.1 \leq \beta \leq 0.2$ as well as the singular index $0.63 \leq \lambda \leq 0.75$ [13, 31].

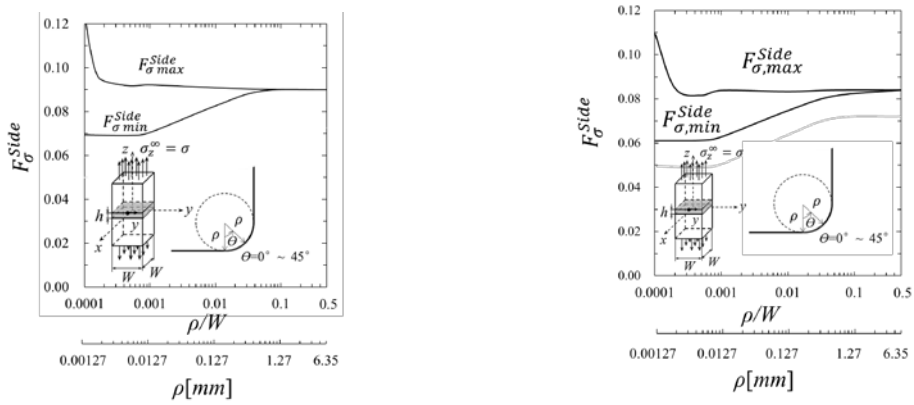

(a) For Steel/Resin A (b) For Steel/Resin B

Fig. 6 $F_{\sigma\,max}^{Side}$ vs. ρ/W relation and $F_{\sigma\,min}^{Side}$ vs. ρ/W relation

2.3 ISSF variation due to thermal loading

Since electric device failures are often caused by thermal stress, the thermal ISSF should be discussed. Singular stress appears because of the mismatch of dissimilar materials having different thermal expansion coefficient. In this section, the thermal ISSF is considered in Fig. 7 under the temperature change $T \rightarrow T+\Delta T$. It is known that the thermal stress σ_z^T includes a non-singular term σ_{0T} as described in [23, 24]. The singular term $(\sigma_z^T - \sigma_{0T})$ has a singularity of the form $r^{1-\lambda}$ as shown in Eqs. (6)- (8). Table 3 shows the coefficient of thermal expansion α^T.

$$\sigma_z^T - \sigma_{0T} = \lim_{r \to 0} \frac{K_\sigma^T}{r^{1-\lambda}} \tag{6}$$

$$\sigma_{0T} = -\Delta\alpha^T \Delta E \Delta T \tag{7}$$

where,

$$\Delta\alpha^T = (1+\nu_1)\alpha_1^T - (1+\nu_2)\,\alpha_2^T \tag{8}$$

$$\Delta E = \frac{8}{\left\{\frac{(\kappa_1 - 3)}{G_1} - \frac{(\kappa_2 - 3)}{G_2}\right\}}, \tag{9}$$

$$G_j = \frac{E_j}{2(1+\nu_j)} \quad (j = 1: \text{Adherend}, j = 2: \text{adhesive}) \tag{10}$$

Dimensionless thermal ISSF can be defined by Eq. (3).

$$F_\sigma^{Thermal} = \frac{K_\sigma^T}{\sigma_{0T} W^{1-\lambda}} \tag{11}$$

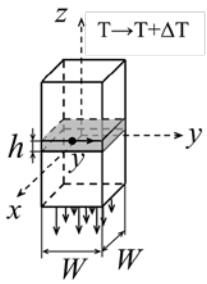

Fig. 7 Prismatic butt joint affected by temperature difference

Table 3 Coefficient of thermal expansion

	Material	α^T ($\times 10^{-5}$[/°C])
Adherend	S35C	12.2
Adhesive	Epoxy resin	5.5

Table 4 FEM stress $\sigma_{z,FEM}^T - \sigma_{0T}$ and FEM stress ratio $(\sigma_{z,FEM}^T - \sigma_{0T})/\sigma_{z\,FEM}^{2D}|_{h/W\geq 1}$

	$e_{\min}$=1/2000mm		$e_{\min}$=1/8000mm	
y/W	$\sigma_{z,FEM}^T - \sigma_{0T}$	$\frac{\sigma_{z,FEM}^T - \sigma_{0T}}{\sigma_{z\,FEM}^{2D}\|_{h/W\geq 1}}$	$\sigma_{z,FEM}^T - \sigma_{0T}$	$\frac{\sigma_{z,FEM}^T - \sigma_{0T}}{\sigma_{z\,FEM}^{2D}\|_{h/W\geq 1}}$
0	-0.788	-0.0811	-1.221	-0.0811
0.1	-0.788	-0.0811	-1.221	-0.0811
0.2	-0.789	-0.0812	-1.222	-0.0812
0.3	-0.790	-0.0813	-1.224	-0.0813
0.4	-0.792	-0.0815	-1.227	-0.0815
0.49	-0.723	-0.0744	-1.123	-0.0746
θ=0°	-0.723	-0.0744	-1.123	-0.0746

θ=15°	-0.727	-0.0748	-1.132	-0.0751
θ=30°	-0.724	-0.0745	-1.127	-0.0748
θ=45°	-0.723	-0.0743	-1.124	-0.0747

Since the same singular stress fields appears around the singular points, the thermal ISSF can be obtained from the FEM stress ratio by applying the same mesh pattern to the unknown and the reference problems as shown in Eq. (12).

$$\frac{K_\sigma}{K_\sigma^*} = \frac{\sigma_{z,FEM}^T - \sigma_{0T}}{\sigma_{z,FEM}^*} \tag{12}$$

Here, the superscript* denotes the reference problem. Table 4 shows the values of $(\sigma_{z,FEM}^T - \sigma_{0T})$ obtained by FEM by varying minimum mesh size. As the reference problem, the two-dimensional bonded plate $\sigma_{z\,FEM}^{2D}\,|_{\,h/W\geq 1}$ is used in Table 4, since the exact solution is available [23, 24]. Although the value of $(\sigma_{z,FEM}^T - \sigma_{0T})$ is depending on the mesh size, the stress ratio $(\sigma_{z,FEM}^T - \sigma_{0T})/\,\sigma_{z,FEM}^*$ is mesh-independent.

Fig. 8 and Table 5 show the normalized thermal ISSF variation $F_\sigma^{Thermal}$. As shown in Fig. 8 and Table 5, thermal ISSF $F_\sigma^{Thermal}$ coincides with the ISSF F_σ^{Side} under tension within 1% error. Since the thermal ISSF appears in a similar way of the ISSF under tension, this paper's discussion is useful for understanding thermal failure.

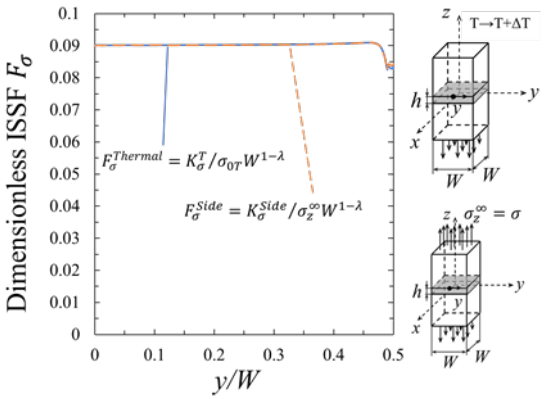

Fig. 8 Dimensionless ISSF distribution

Table 5 Normalized thermal ISSF $F_\sigma^{Thermal}$ and Normalized ISSF under tension F_σ^{Side} when ρ/W=0.01 and h/W=0.01

y/W	$F_\sigma^{Thermal}=\frac{K_\sigma^T}{\sigma_{0T}W^{1-\lambda}}$	$F_\sigma^{Side}=\frac{K_\sigma^{Side}}{\sigma_z^\infty W^{1-\lambda}}$
0	0.0902	0.0900
0.1	0.0902	0.0902
0.2	0.0903	0.0902
0.3	0.0904	0.0903
0.4	0.0907	0.0906
0.49	0.0829	0.0836
θ=0°	0.0829	0.0836
θ=15°	0.0834	0.0842
θ=30°	0.0831	0.0839
θ=45°	0.0829	0.0837

3. Fracture origin identification based on the ISSF

3.1 Suzuki's experimental method

As shown in Table 1, two types adhesives were used in the experiment [17]. Resin A is a brittle bisphenol-A-type epoxy resin Epikote 828. Resin B is a ductile resin prepared by adding the dimer-acid-type flexible epoxy Epikote 871 to Resin A. Fig. 9 shows the shape and dimensions of the butt joint specimen. The adherend is medium carbon steel JIS S35C. The adhesive surface is the square with 12.7mm × 12.7mm and the bondline thickness h varies as h = 0.05~5.0mm. Adhering surfaces are ground mechanically by using WAH 60 (white aluminum oxide, No.60 grain size) grinding wheel. The grinding direction (wheel rotating direction) coincides with the longitudinal direction of the specimens. Subsequently, 10-minute ultrasonic cleaning with trichloroethylene is applied four times. Since the adhesive absorbs moisture, the adhesive strength tends to decrease with large scattering. Therefore, the following bonding method is adopted. The pair of adherends are fixed by using a jig with a distance between both adhesive surfaces so that the bondline thickness h can be achieved. After

the adhesive is degassed in vacuum, the adhesive is dropped on the bonded portion placed in a vacuum desiccator by using an injector. After the vacuum impregnation of adhesive, the specimen is placed in a silica gel-containing desiccator about 24 hours until the adhesive is nearly cured. The curing time for adhesives is 14 days at room temperature. The adhesive protruding to the edge of the adhesive layer is removed by polishing with emery paper (from #400 to #1000). The polishing direction was parallel to the longitudinal direction.

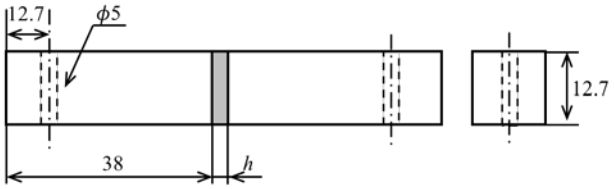

Fig. 9 Dimension of specimens (Units : mm)

3.2 Fracture origin at the surface

Fig. 10 illustrates the fracture surfaces for the small bondline thickness (a) h =0.05, (b) h =0.1, (c) h =0.3 (h/W = 0.00394 ~ 0.0236). As shown in Fig. 10, the fracture originating regions are also indicated for Steel/Resin A. Although the debonding condition of Steel/Resin B can be expressed as ISSF constant as well as Steel/Resin A [14], the fracture origin for Steel/Resin B cannot be identified clearly because no specific fracture pattern can be seen. Therefore, the fracture origin for Steel/Resin A in Table 1 is focused in this paper.

In Fig. 10, the left figures show the entire fracture surface with the middle and right figures showing the detail. Fig. 10 (a)-(c) includes enlarged views (×100) and Fig. 10 (b), (c) also includes more enlarged view (×1000). In Fig.10 (a), the fractures originate from the interface corner. However, in Fig.10 (b) and (c), the fractures originate from the interface side away from the corners [25]. In this study, five specimens are investigated for each h. Out of total 35 (=5×7) specimens, only one specimen

shown in Fig.10 (a), the fracture originates from the interface corner. In other 34 specimens, the fracture originates from the interface side.

For the bondline thickness h≤0.3mm (h/W≤0.0236), the fracture always originates at the interface edge as shown in Fig. 10 (a)-(c). In Fig. 10 (b), (c), microcracks about 20μm depth can be seen at the adhesive surface at $|x|=W/2$ in Fig. 1 (a). Those cracks are formed due to the machining the xy plane at $|z|=h/2$ before bonding in the y-direction in Fig. 1 (a). Since the yz surface of Fig.1(a) at $|x|=W/2$ is polished in the z-direction by using sandpaper from # 400 to # 1000, microcracks may be formed affected by those machining and polishing at the intersection $|x|=W/2$ and $|z|=h/2$. It may be conjectured that those microcracks can be origins of the fracture.

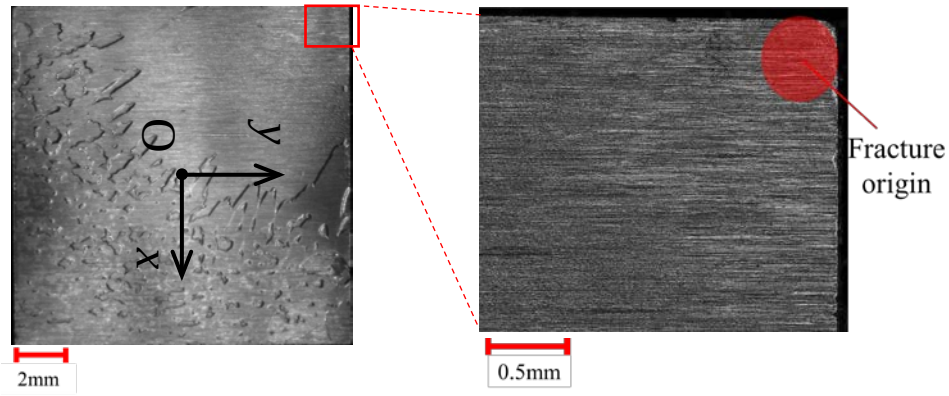

(a1) ×20 (a2) ×100

(a) h/W=0.00394 (h=0.05mm) for the bonded xy surface at $|z|\leq h/2$ in Fig. 1 (a)

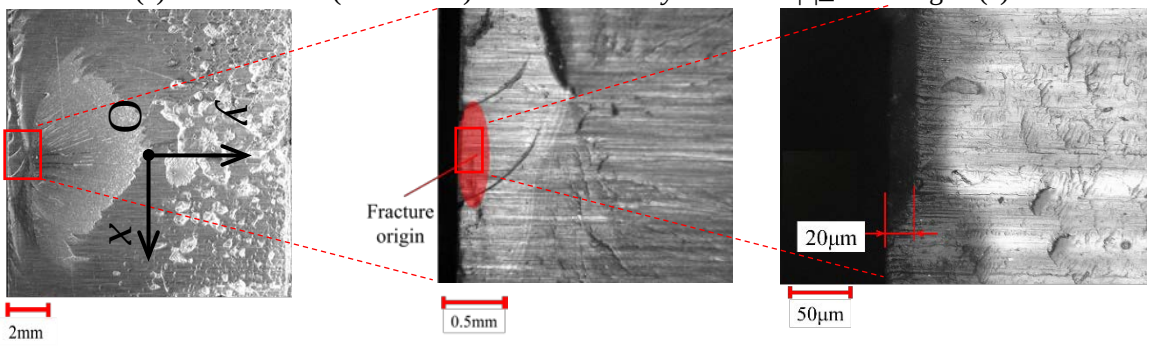

(b1) ×20 (b2) ×100 (b3) ×1000

(b) h/W=0.00787 (h=0.1mm) for the bonded xy surface at $|z|\leq h/2$ in Fig. 1 (a)

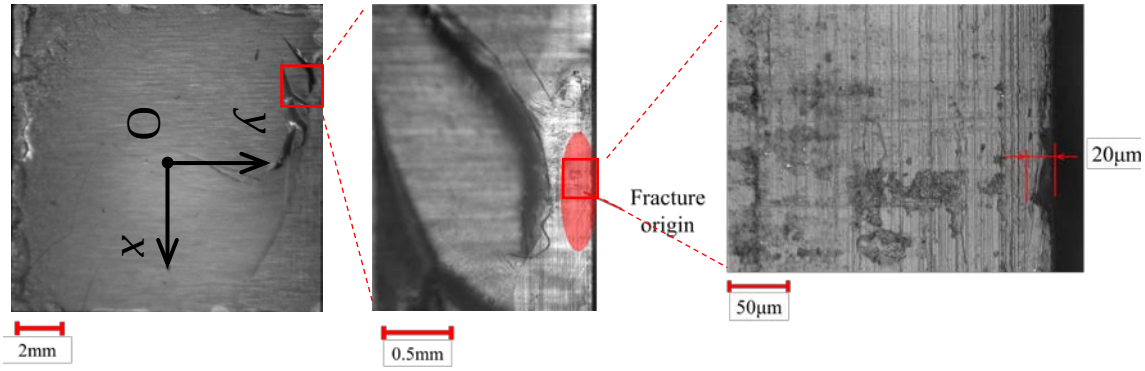

(c1) ×20 (c2) ×100 (c3) ×1000

(c) h/W=0.0236 (h=0.3mm) for the bonded xy surface at $|z|\leq h/2$ in Fig. 1 (a)

Fig. 10 The fracture surface for $h\leq$0.3mm whose ISSF is indicated in Fig.14 and Fig.15

3.3 Fracture origin near the surface

Fig. 11 illustrates the fracture surfaces for the large bondline thickness (a) h =0.6, (b) h =1.0, (c) h =2.0, (d) h=5.0mm (h/W = 0.0472 ~ 0.394). In Fig. 11, the left figures show the entire fracture surface with the right figures showing the enlarged views (×100). As shown in Fig. 11(a)-(d), the fracture pattern from sub-surface can be seen. When the bondline thickness $h\geq$0.6mm ($h/W\geq$0.0472), it may be conjectured that the fracture originates at the sub-surface about 0.5mm away from the edge.

Fig. 12 shows an example of a void found in the adhesive layer. The void's diameter is from 10μm to 200μm as shown in Fig. 11. Although the Suzuki's specimens were carefully prepared by excluding air bubbles as described in Section 3.1, those voids are sometimes found for the large bondline thickness $h\geq$1.0mm. However, the voids do not affect the fracture since the stress concentration factor of the spherical void is 2.045 [26] much smaller than the singular stress at the interface end.

Fig. 13 illustrates the triaxiality factor η along the middle of the interface (x, y, z)=(0, y, $\pm h/2$) in

Fig. 1 (a) obtained by FEM by using the averaged values at nodes. The triaxiality factor η is defined from principal stresses $\sigma_1, \sigma_2, \sigma_3$ as equation (5).

$$\eta = \frac{3\sigma_m}{\sigma_{eq}} = \frac{\sqrt{2}(\sigma_1 + \sigma_2 + \sigma_3)}{\sqrt{(\sigma_1 - \sigma_2)^2 + (\sigma_2 - \sigma_3)^2 + (\sigma_3 - \sigma_1)^2}} \tag{5}$$

This triaxiality factor η is the ratio of hydrostatic to octahedral shearing stresses [27]. The triaxiality factor η=+2 for equal biaxial tension, η=+1 for uniaxial tension, η=0 for pure shear, and η=−1 for uniaxial compression. The magnitude of the load required for yielding increases with increasing the triaxiality factor η [28]. As shown in Fig. 11, at the 0.5mm inside the surface at *y*/*W*=0.45, it can be seen that the triaxiality factor η decreases with increasing the bondline thickness *h*. Therefore, when the large bondline thickness, since the triaxiality η is smaller and the deformation can be larger inside, the fracture originates often around the 0.5mm inside from the edge. Instead, when the small bondline thickness, since the triaxiality η is smaller only at the edge, the fracture originates at the interface edge.

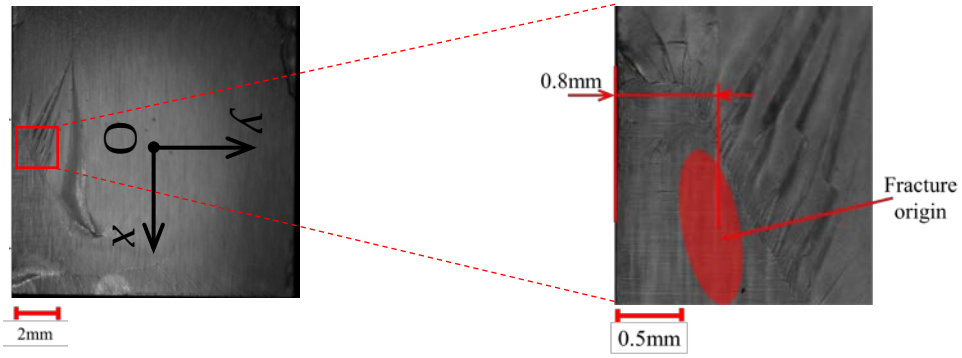

(a) *h*/*W*=0.0472 (*h*=0.6mm) for the bonded *xy* surface at |*z*|≤*h*/2 in Fig. 1 (a)

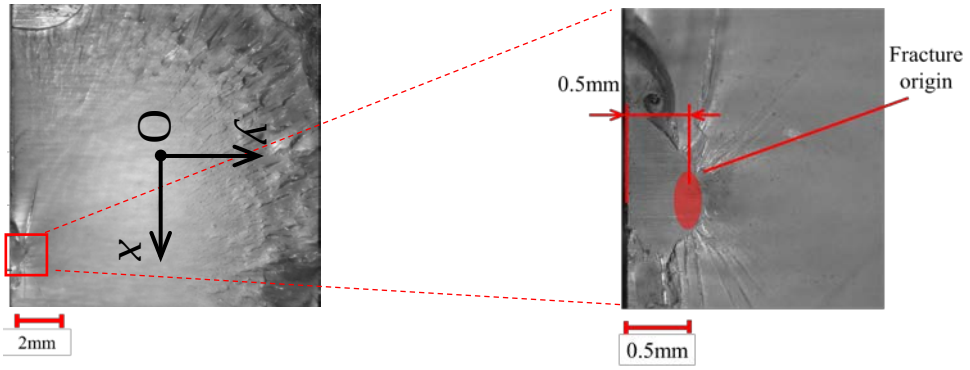

(b) h/W=0.0787 (h=1.0mm) for the bonded xy surface at $|z|\leq h/2$ in Fig. 1 (a)

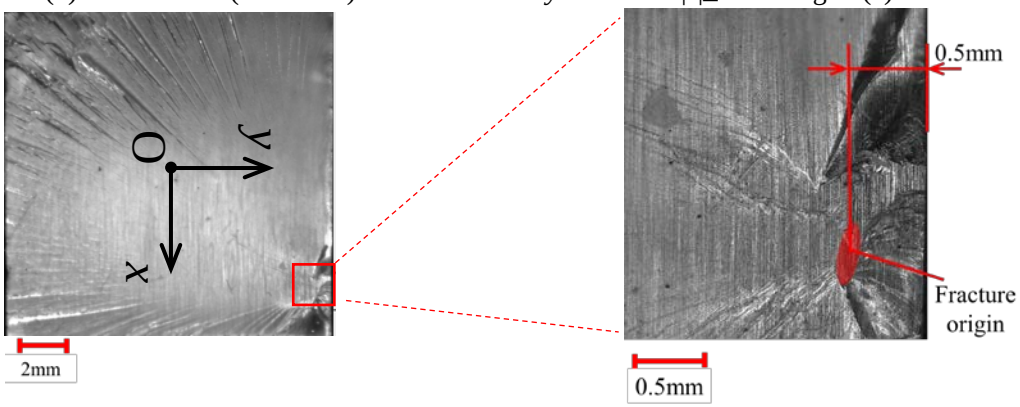

(c) h/W=0.157 (h=2.0mm) for the bonded xy surface at $|z|\leq h/2$ in Fig. 1 (a)

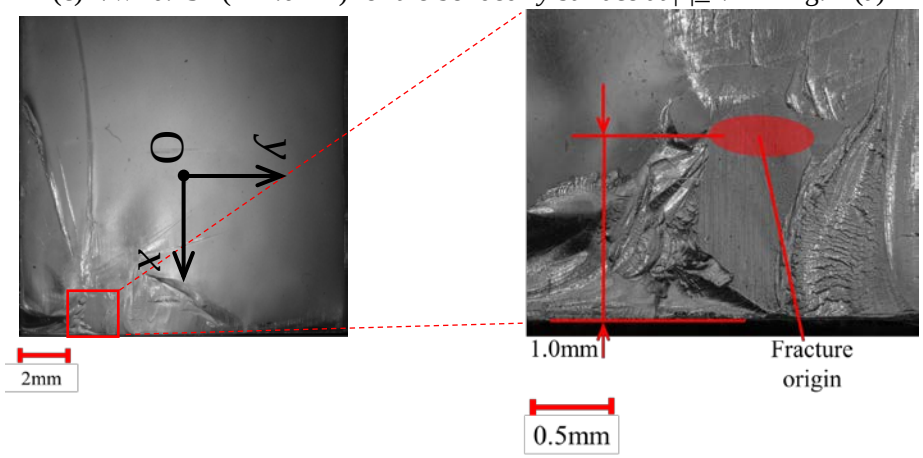

(d) h/W=0.394 (h=5.0mm) for the bonded xy surface at $|z|\leq h/2$ in Fig. 1 (a)

Fig.11 The fracture surface for $h\geq$0.6mm whose ISSF is indicated in Fig.14 and Fig.15

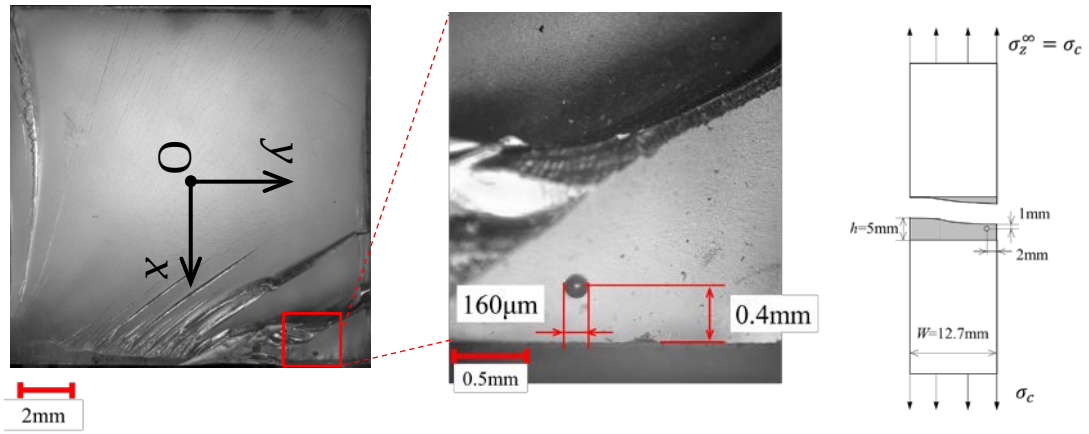

(a) ×20 (b) ×300 (c) The position of void

Fig. 12 Example of voids observed in large adhesive layer h=5.0mm

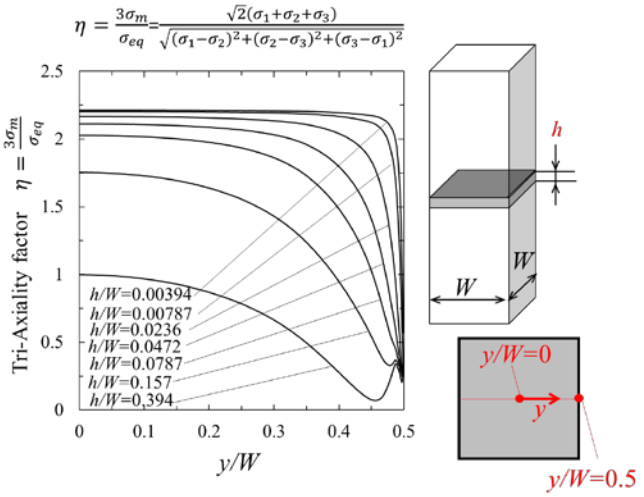

Fig. 13 Tri-axiality factor η by obtaining FEM along the x=0 line in the interface

3.4 Fracture origin in relation to the ISSF

By considering the chamfering dimension in Fig.2, the corner fillet radius ρ= 0.127mm (ρ/W= 0.01) is used to analyze the ISSF of the butt joint in Fig.2. Under remote tensile stress σ_z^∞ = 1MPa, Fig. 14 (a) shows the ISSF variations for y/W=0~0.5 when h=0.05mm~ 5.0mm (h/W =0.00394 ~ 0.394). Fig. 14 (b) shows the detail ISSF variation for y/W = 0.45~0.5. With decreasing h/W, the ISSF decreases.

This is because the singular stress fields along the two interface circumferences interact each other and reduce the ISSF. Under fixed h, as shown in Fig. 14, the ISSF is almost constant at the middle of the interface side. Under debonding stress $\sigma_z^{\infty} = \sigma_c$, Fig. 15 shows the critical ISSF variations with the fracture origins denoted by the solid circles. Here, the fracture origins are plotted for five specimens under fixed h/W [17]. When the origin cannot be specified, the central point of the fracture starting region is plotted.

From Fig. 14 and Fig. 15, it is seen that the maximum ISSF at the side is almost equal to the maximum ISSF at the corner when $h \leq 2.0$ mm ($h/W \leq 0.157$). However, most of the fractures originate from the interface side instead of the interface corner because the maximum ISSF exists in a certain range at the middle of the interface side. Instead, the maximum ISSF always exists in a limited region at the interface corner and the fracture hardly occurs at the corner. The peak ISSF appears reflecting the corner point singularity at $y/W = 0.5$ when $\rho \rightarrow 0$. The fracture origin is found at the corner only for the smallest h = 0.05mm (h/W = 0.00394) as shown in Fig. 10(a) when the ISSF variation is almost constant as shown in Fig. 14 (b).

Fig. 16 shows the example of the fracture surface where the fracture origin looks being located near the corner for the bondline thickness h=0.1mm. However, the detail observation in Fig.16 (b) shows the facture point at the corner is not located at the vertex as shown in Fig. 16 (c). Therefore, it may be concluded that the peeling was progressed toward the corners in this case. It can be concluded that most of the fracture originates from the interface side instead of the interface corner because the maximum ISSF exists in a limited region at the interface corner although the ISSF at the interface side is equal to the ISSF at the corner when $h \leq 2.0$ mm ($h/W \leq 0.157$).

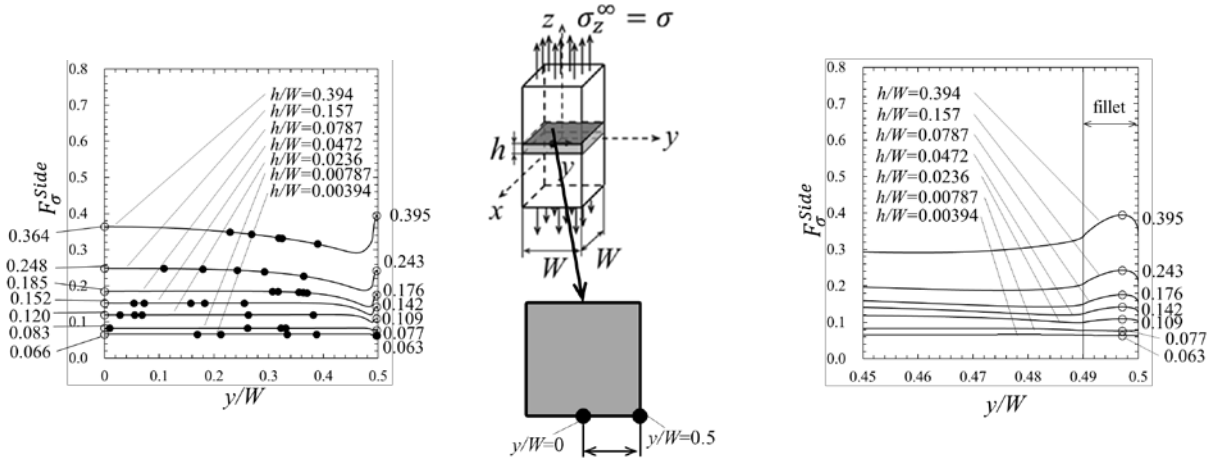

(a) ISSF for $0 \le y/W \le 0.5$ (b) ISSF for $0.45 \le y/W \le 0.5$

Fig. 14 ISSF variations by varying adhesive thickness

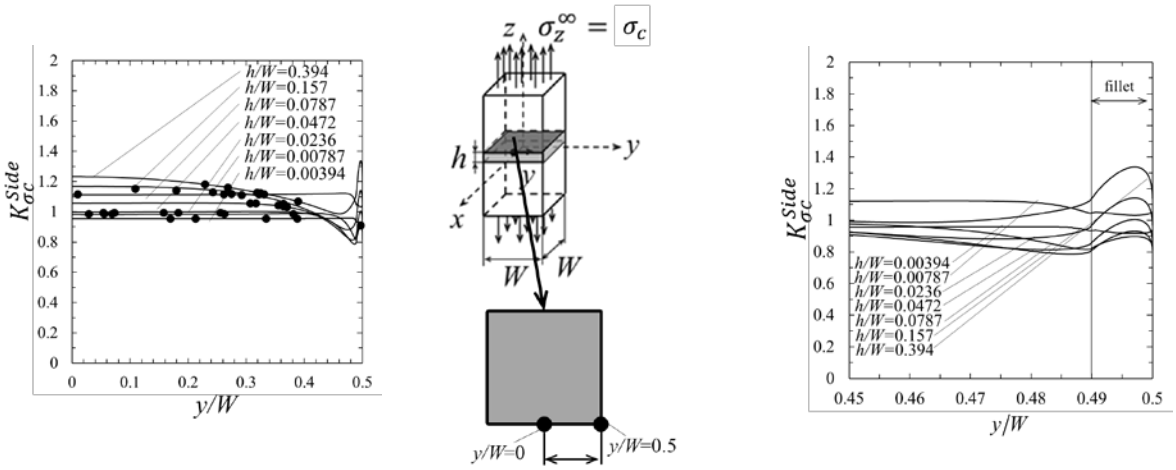

(a) ISSF for $0 \le y/W \le 0.5$ (b) ISSF for $0.45 \le y/W \le 0.5$

Fig. 15 Critical ISSF distributions by varying adhesive thickness

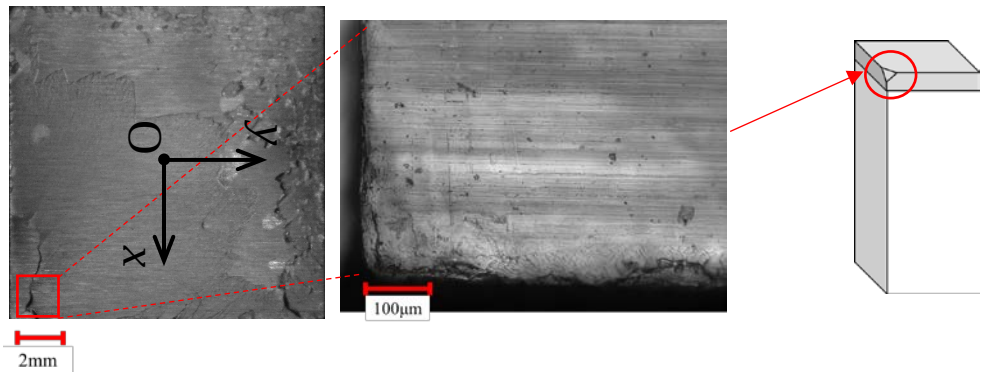

(a) ×20 (b) ×300 (c) Illastration of adhesive surfece around the corner

Fig. 16 Enlarged view of fracture surface around the corner when h=0.1mm

4. Conclusion

In this study, the detail fractographic observation was conducted to identify the fracture origin for the prismatic butt joints whose debonding condition can be expressed as a constant value of the ISSF. The discussion is based on the ISSF variation newly analyzed by considering the three-dimensional shape of prismatic butt joints with corner fillet. The critical ISSF value was clarified where the fracture occurs to understand how the debonding occurs. The conclusions obtained are summarized as follows.

(1) The ISSF variation analysis showed that the maximum ISSF appears at $y/W \cong 0.46$ in Fig.4 and Fig.5. The minimum value of ISSF appears at $y/W \cong 0.498$ independent of ρ/W. The maximum ISSF value $F_{\sigma,max}^{Side}$ is almost the same independent of ρ/W within 2% variation in the range $\rho/W \geq 0.0005$ ($\rho \geq 0.00635mm$). The ISSF variations for Steel/ Resin A and Steel/Resin B are nearly the same within 9% error.

(2) The detail fractographic observation showed that most of the fracture originates from the maximum ISSF region of the interface edge as shown in Fig.10 and Fig. 11. Out of total 35 specimens, only one specimen's fracture starts from the interface corner and other 34 specimens' fractures start from the interface edge.

(3) When the bondline thickness $h \leq 2.0$ mm ($h/W \leq 0.157$), the maximum ISSF at the middle of the interface side coincides with the ISSF at the corner. Although the maximum ISSF exists in a certain range near the middle of the interface side, the maximum ISSF exists only in a limited region at the interface corner. This is the reason why the fracture hardly occurs at the corner.

(4) The fractographic observation showed that for smaller bondline thickness $h \leq 0.3$mm ($h/W \leq 0.0236$), the fracture originates from microcracks about 20μm depth at the interface edge. Those

microcracks are formed due to the machining the *xy* plane at $|z|=h/2$ and the polishing the *yz* surface $|x|=W/2$ in Fig.1 (a).

(5) The fractographic observation showed that for larger bondline thickness $h \geq 0.6$mm ($h/W \geq 0.0472$) the fracture originates at the sub-surface located about 0.5mm away from the edge. This is because the stress triaxiality decreases at the sub-surface causing larger deformation when the bondline thickness *h* is larger.

(6) The ISSF $F_{\sigma}^{Thermal}$ due to thermal loading is the same as ISSF F_{σ}^{Side} under tension. Therefore, similar fracture origin can be expected under thermal loading. In other words, the discussion of the fracture origin under tension discussed in this paper is useful for under thermal loading.

Appendix A: Experimentally obtained adhesive strength controlled by the ISSF

Table A1(a) shows the original experimental results expressed as the remote tensile stress σ_c obtained by Suzuki for Fig.1 (a) [17]. Table A1(b), Table A1(c) and Table A1(d) show the ISSFs discussed in the previous papers [14, 16, 25]. As shown in Table A1(a), the original experimental data include about 10% scatter under the fixed adhesive thickness *h*. Table A1(b) and Table A1(c) show that the ISSF $K_{\sigma c}^{2D}$ and $K_{\sigma c}^{Side}$ may predict the adhesive strength within 7% error for S35C/Epoxy Resin A and within 12% error for S35C/Epoxy Resin B independent of adhesive thickness *h*. On the other hand, Table A1 (d) shows that the ISSF at the vertex $K_{\sigma c}^{vtx}$ in Table A1 (d) may predict the adhesive strength within 21% error for S35C/Epoxy Resin A and 13% error for S35C/Epoxy Resin B independent of adhesive thickness *h*.

Table A1 Experimentally and analytically obtained adhesive strength

(a) Adhesive strength expressed by for remote tensile stress

		(i) S35C/Epoxy Resin A						(ii) S35C/Epoxy Resin B			
		Strength						Strength			
h	*h/W*	Debonding strength σ_c[MPa]					Average ± SD[MPa]	Debonding strength σ_c[MPa]			Average ± SD[MPa]
0.05	0.00394	47.7	50.0	58.4	63.5	66.5	57.2 ± 7.34	72.8	77.6	79.9	76.8 ± 2.96
0.10	0.00787	44.3	49.8	52.0	57.0	63.5	53.3 ± 6.52	70.2	71.5	72.6	71.4 ± 0.98
0.30	0.0236	28.6	30.8	32.5	34.2	36.5	32.5 ± 2.72	45.5	50.9	52.6	49.7 ± 3.03
0.60	0.0472	21.9	24.8	25.2	28.2	29.6	25.9 ± 2.71	39.6	40.0	43.9	41.2 ± 1.94
1.00	0.0787	21.5	21.5	21.9	23.5	24.4	22.6 ± 1.18	21.1	26.5	28.4	25.3 ± 3.09
2.00	0.157	14.8	18.1	18.2	19.9	20.9	18.4 ± 2.08	18.1	19.7	21.3	19.7 ± 1.31
5.00	0.394	11.4	11.4	13.6	15.0	15.6	13.4 ± 1.76	12.4	12.4	16.0	13.6 ± 1.70

SD : Standard deviation

(b) Adhesive strength expressed by ISSF obtained by 2D modelling

	(i) S35C/Epoxy Resin A			(ii) S35C/Epoxy Resin B		
h/W	σ_c[MPa]	F_σ^{2D}	$K_{\sigma c}^{2D}$[MPa·m$^{0.315}$] Average ± SD	σ_c[MPa]	F_σ^{2D}	$K_{\sigma c}^{2D}$[MPa·m$^{0.326}$] Average ± SD
0.00394	57.2	0.0671	0.970 ± 0.125	76.8	0.0620	1.147 ± 0.044
0.00787	53.3	0.0831	1.120 ± 0.137	71.4	0.0778	1.339 ± 0.018
0.0236	32.5	0.119	0.978 ± 0.082	49.7	0.112	1.342 ± 0.082
0.0472	25.9	0.150	0.981 ± 0.102	41.2	0.142	1.411 ± 0.066
0.0787	22.6	0.178	1.017 ± 0.053	25.3	0.171	1.042 ± 0.127
0.157	18.4	0.231	1.071 ± 0.121	19.7	0.223	1.060 ± 0.070
0.394	13.4	0.335	1.135 ± 0.149	13.6	0.331	1.085 ± 0.135
$K_{\sigma c(average)}$			1.039 ± 0.064			1.204 ± 0.144

(c) Adhesive strength expressed by ISSF obtained by 3D modelling at the interface side

	(i) S35C/Epoxy Resin A			(ii) S35C/Epoxy Resin B		
h/W	σ_c[MPa]	F_σ^{Side}	$K_{\sigma c}^{Side}$[MPa·m$^{0.315}$] Average ± SD	σ_c[MPa]	F_σ^{Side}	$K_{\sigma c}^{Side}$[MPa·m$^{0.326}$] Average ± SD
0.00394	57.2	0.0669	0.966 ± 0.139	76.8	0.0619	1.144 ± 0.054
0.00787	53.3	0.0840	1.130 ± 0.155	71.4	0.0783	1.346 ± 0.023
0.0236	32.5	0.120	0.989 ± 0.093	49.7	0.114	1.361 ± 0.102
0.0472	25.9	0.151	0.983 ± 0.115	41.2	0.144	1.428 ± 0.082

0.0787	22.6	0.185	1.055 ± 0.062	25.3	0.178	1.082 ± 0.162
0.157	18.4	0.245	1.138 ± 0.144	19.7	0.239	1.132 ± 0.092
0.394	13.4	0.338	1.144 ± 0.168	13.6	0.334	1.094 ± 0.167
$K_{\sigma c(average)}$			1.058 ± 0.080			1.227 ± 0.146

(d) Adhesive strength expressed by ISSF obtained by 3D modelling at the interface corner

	(i) S35C/Epoxy Resin A			(ii) S35C/Epoxy Resin B		
h/W	σ_c[MPa]	F_σ^{vtx}	$K_{\sigma c}^{vtx}$[MPa·m$^{0.392}$] Average ± SD	σ_c[MPa]	F_σ^{vtx}	$K_{\sigma c}^{vtx}$[MPa·m$^{0.404}$] Average ± SD
0.00394	57.2	0.0380	0.392 ± 0.056	76.8	0.0347	0.457 ± 0.022
0.00787	53.3	0.0502	0.482 ± 0.066	71.4	0.0462	0.565 ± 0.010
0.0236	32.5	0.0782	0.458 ± 0.043	49.7	0.0729	0.621 ± 0.046
0.0472	25.9	0.104	0.487 ± 0.057	41.2	0.0982	0.694 ± 0.040
0.0787	22.6	0.131	0.532 ± 0.031	25.3	0.124	0.539 ± 0.081
0.157	18.4	0.183	0.606 ± 0.077	19.7	0.177	0.596 ± 0.048
0.394	13.4	0.300	0.724 ± 0.106	13.6	0.297	0.691 ± 0.106
$K_{\sigma c(average)}$			0.526 ± 0.109			0.595 ± 0.078

Appendix B: How to obtain the ISSF variation

The previous studies [13-16, 29] described the ISSF analysis method to evaluate the adhesive strength. In this study, therefore, how to obtain the ISSF is briefly described. The fracture origin was identified on the basis of the ISSF newly analyzed for Fig. 2. To obtain mesh-independent ISSF, the proportional method is applied by using the same FEM mesh pattern to the reference and unknown problems [13-16, 21]. Fig. B1 illustrates the analysis model having the corner fillet radius ρ. Fig. B1 illustrates FEM model for one-eighth region of the prismatic butt joint in Fig.1 (a). From the symmetry, the boundary conditions are applied as u_x=0 at x=0, u_y=0 at y=0 and u_z=0 at z=0 in Fig. 1(a). By considering the real chamfer dimension in Fig.3, ρ=0.0127mm (ρ/W=0.01) is mainly focused; however, to understand the fillet radius effect ρ=0~6.35mm (ρ/W=0~0.5) is also discussed. By considering the experiment [17], h =0.5~5.0mm is analyzed. First, the main model in Fig. B1 (a) consisting of larger

elements is analyzed to obtain the displacements. Next, the submodel in Fig. B1 (b) consisting of smaller elements is analyzed by using the obtained displacement. The ISSF is calculated from the submodel confirming mesh-independency [16]. The analysis model is composed of 8-node hexahedral elements as shown in Fig. B1. A commercially available MSC Marc/Mentat 2012 is used as the analysis code in this study.

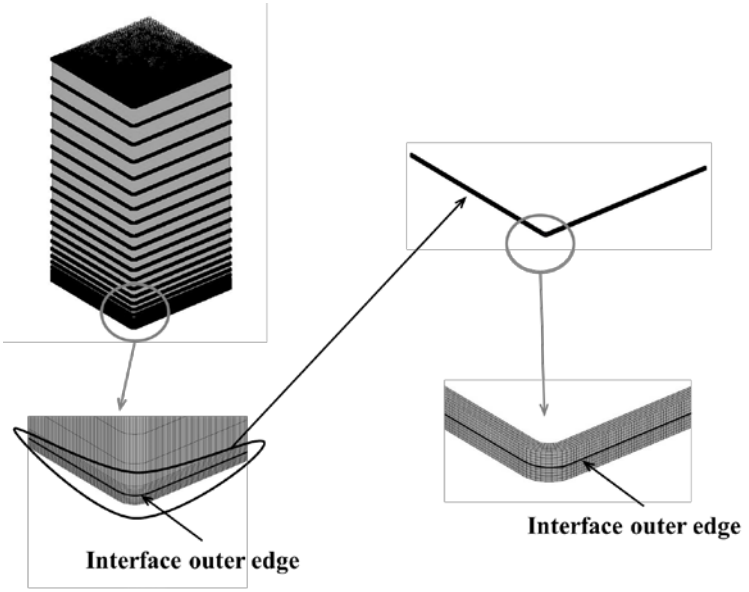

(a) Coarsely meshed model (b) Finely meshed submodel

Fig. B1 FEM model for one-eighth region of the prismatic butt joint in Fig.1 (a)

Since the FEM stress $\sigma_{z\,FEM}^{Side}$ varies depending on the mesh size, the ISSF cannot be obtained from Equations (1) and (2). However, by applying the same mesh pattern to the unknown and the reference problems around the interface edge, the FEM stress ratio can be mesh-independent as shown in the previous study [16]. This is because the error of the FEM stress ratio can be canceled under the same mesh [13, 14]. The exact ISSF of the unknown problem can be obtained by multiplying the FEM stress ratio and the exact ISSF of the reference solution. The following relationship can be confirmed from the reference problem (K_σ^{REF}, F_σ^{REF}, $\sigma_{z\,FEM}^{REF}(r)$) and the unknown problem (K_σ^{Side}, F_σ^{Side},

$\sigma_{z\,FEM}^{Side}(r)$). Here, λ and σ_z^{∞} are the same for the reference problem and the unknown problem.

$$\frac{K_\sigma^{Side}}{K_\sigma^{REF}} = \frac{F_\sigma^{Side}\sigma_z^{\infty}W^{1-\lambda}}{F_\sigma^{REF}\sigma_z^{\infty}W^{1-\lambda}} = \frac{\lim_{r\to 0}\left[r^{1-\lambda}\times\sigma_{z\,Real}^{Side}(r)\right]}{\lim_{r\to 0}[r^{1-\lambda}\times\sigma_{z\,Real}^{REF}(r)]} = \lim_{r\to 0}\frac{r^{1-\lambda}\times\sigma_{z\,Real}^{Side}(r)}{r^{1-\lambda}\times\sigma_{z\,Real}^{REF}(r)} = \frac{\sigma_{z\,FEM}^{Side}(r)}{\sigma_{z\,FEM}^{REF}(r)} \quad (13)$$

$$\text{but } \sigma_z^{Side,FEM} \neq \sigma_z^{Side,Real}$$

Table B1 shows an example of the FEM stress ratio based on small strain-small displacement analysis. Here, the two-dimensional bonded plate whose exact solution is available can be used as the reference problem. Table B1 (a) shows FEM stress ratio $\sigma_{z\,FEM}^{Side}|_{h/W=0.01}/\sigma_{z\,FEM}^{2D}|_{h/W\geq 1}$ along the interface side. Table B1 (b) shows the FEM stress ratio $(\sigma_{z\,FEM}^{Side}|_{h/W=0.01} - \tilde{\sigma}_{z\,FEM}^{Side})/\sigma_{z\,FEM}^{2D}|_{h/W\geq 1}$ around the corner fillet. It is known that the non-singular term $\tilde{\sigma}_{z\,FEM}^{Side}$ appears at the corner fillet, which is expressed by Eq. (14) [29, 30].

$$\tilde{\sigma}_{z\,FEM}^{Side} = -\frac{(\nu_1-\nu_2)E_1E_2}{(1+\nu_1)\nu_1E_2-(1+\nu_2)\nu_2E_1}\varepsilon_\theta \quad (14)$$

Here, ε_θ is the strain in the θ-direction in Fig. 2. As shown in Table B1, the ratio of FEM stress is mesh-independent at the straight interface side and the corner fillet. As shown in Table B1, the ISSF can be obtained accurately from the ISSF ratio.

Table B1 Mesh independency of FEM stress ratio (ρ/W=0.01, h/W=0.0236)

(a) At straight interface side

y/W	$\frac{\sigma_{z\,FEM}^{Side}\|_{h/W=0.01}}{\sigma_{z\,FEM}^{2D}\|_{h/W\geq 1}}$	
	e_{min}=1/4000mm	e_{min}=1/8000mm
0.000	0.291	0.289
0.100	0.291	0.290
0.200	0.292	0.290
0.300	0.292	0.291
0.400	0.294	0.292
0.450	0.290	0.288
0.490	0.244	0.243

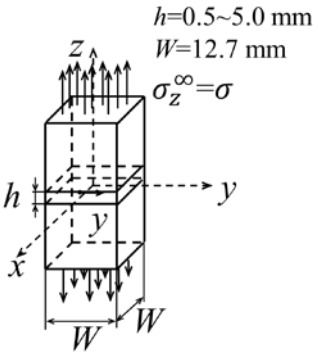

(b) At corner fillet

θ	$\dfrac{\sigma_{z\,FEM}^{Side}\mid_{h/W=0.01} - \tilde{\sigma}_{z\,FEM}^{Side}}{\sigma_{z\,FEM}^{2D}\mid_{h/W\geq 1}}$	
	e_{min}=1/4000mm	e_{min}=1/8000mm
0	0.244	0.243
9	0.252	0.251
18	0.258	0.257
27	0.262	0.261
36	0.265	0.264
45	0.266	0.265

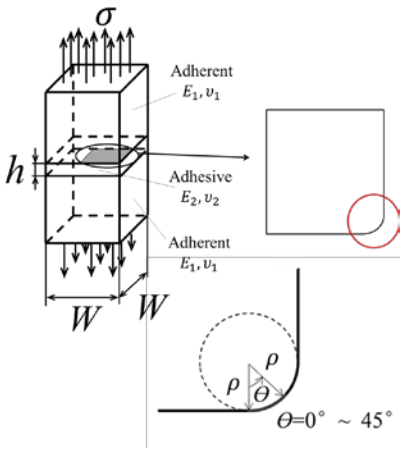

Fig. B2 shows an example of the contour plot of FEM stress for (a) h/W=0.01 and (b) h/W≥1. Fig. B2 (c) shows the FEM stress ratio, which can be regarded as the ISSF ratio. Those figures are useful for understanding the effect of h on the ISSF. As shown in Fig. B2 (a), when h is smaller, FEM stress is comparatively smaller especially at the interface corner due to the interaction of ISSFs at $z=\pm h/2$. Instead, as shown in Fig. B2 (b), when h is larger, FEM stress is larger especially at the corner. With decreasing h, the ISSS decreases due to the interaction of the interfaces $z=\pm h/2$. This is the reason why the debonding strength in Fig.1 (a) can be expressed as a constant ISSF as shown in Fig. 1 (b).

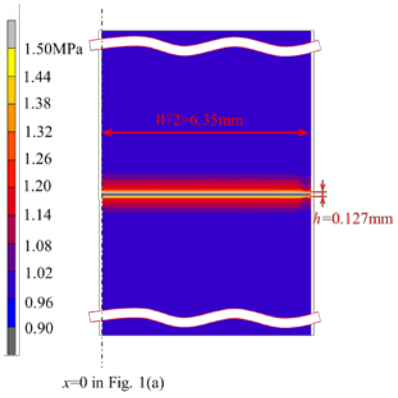

(a)FEM stress σ_z when h/W=0.01 under σ_z^{∞} = 1MPa, e_{min}=1/4000mm

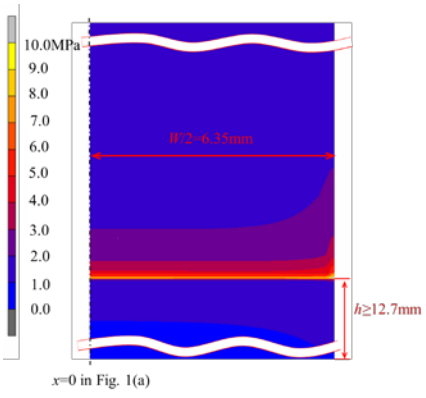

(b)FEM stress σ_z when h/W≥1 under σ_z^{∞} = 1MPa, e_{min}=1/4000mm

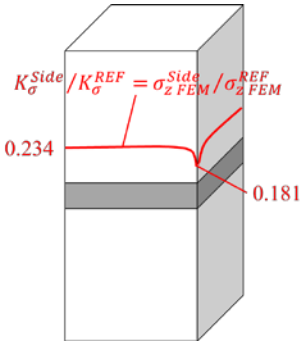

(c) ISSF ratio $K_\sigma^{Side}/K_\sigma^{REF}$ obtained from (a), (b)

Fig. B2 Example of contour plots of FEM Stress σ_z and ISSF ratio distribution

Reference

[1] Adams RD, Coppendale J, Peppiatt NA, Stress analysis of axisymmetric butt joints loaded in torsion and tension, J Strain Analysis Eng Design, 1978; 13(1), 1 –13.

[2] Naito K, Onta M, Kogo Y. The effect of adhesive thickness on tensile and shear strength of polyimide adhesive. Int J Adhes Adhes, 2012; 36, 77 – 85.

[3] Liu ZX, Huang YA, Yin ZP, Bennati S, Valvo PS. A general solution for the two-dimensional stress analysis of balanced and unbalanced adhesively bonded joints. Int J Adhes Adhes, 2014; 54, 112 – 23.

[4] Uddin MA, Ali MY, Chan HP. Achieving optimum adhesion of conductive adhesive bonded flip-chip on flex packages." Reviews on Adv Mater Sci, 2009; 21(2), 165 – 72.

[5] Huang Z, Kumar P, Dutta I, Pang JHL, Sidhu R. A general methodology for calculating mixed mode stress intensity factors and fracture toughness of solder joints with interfacial cracks. Eng Fract Mech, 2014; 131, 9 – 25.

[6] Kitasako Y, Burrow MF, Nikaido T, Harada N, Inokoshi S, Yamada T, Takatsu T. Shear and tensile bond testing for resin cement evaluation. Dental Mater, 1995; 11(5 – 6), 298 – 304.

[7] Kitamura T, Shibutani T, Ueno T. Development of evaluation method for interface strength between thin films and its application on delamination of Su/TaN in an advanced LSI, Trans Jpn Soc Mech Eng A, 2000; 66(648), 1568-73. [in Japanese]

[8] Sibutani T, Tsuruga T, Yu Q, Shiratori M. Criteria of crack initiation at edge of interface between thin films in poening and sliding modes for an advanced LSI, Trans Jpn Soc Mech Eng A, 2003; 69(685), 1368-73. [in Japanese]

[9] Yuki R, Ishikawa H, Kishimoto K, Xu JQ. Mechanics of interface, Baifukan, 1993 [in Japanese]

[10] Qian Z, Akisanya AR. An experimental investigation of failure initiation in bonded joints, Acta Mater, 1998; 46(14), 4895-904.

[11] Akisanya AR, Meng CS. Initiation of fracture at the interface corner of bi-material joints", J Mech Phys Sol, 2003; 51, 27-46.

[12] Mintzas A, Nowell D. Validation of an H_{cr} -based fracture initiation criterion for adhesively bonded joints, Eng Fract Mech, 2012; 80, 13-27.

[13] Zhang Y, Noda NA, Wu P, Duan ML. A mesh-independent technique to evaluate stress singularities in adhesive joints. Int J Adhes Adhes 2015; 57: 105–17; Corrigendum of authorship “A mesh-independent technique to evaluate stress singularities in adhesive joints”. Int J Adhes 2015; 60: 130.

[14] Noda NA, Miyazaki T, Li R, Uchikoba T, Sano Y, Takase Y. Debonding strength evaluation in terms of the intensity of singular stress at the corner with and without fictitious crack. Int J Adhes

2015; 61: 46–64.

[15] Miyazaki T. Inoue T. Noda NA. Practical method for analyzing singular index and intensity of singular stress field for three-dimensional bonded plate", IOP Conf. Series: Mat Sci Eng, 2018; 372(1): 012002.

[16] Takaki R, Noda NA, Ren F, Sano Y, Takase Y, Miyazaki T, Suzuki Y, Lan X. Variation of intensity of singular stress field (ISSF) along the interface outer edge of prismatic butt joint and debonding condition expressed by the ISSF, Int J Adhes Adhes, 2020; 102: 102665.

[17] Suzuki Y. Adhesive Tensile Strengths of Scarf and Butt Joints of Steel Plates (Relation Between Adhesive Layer Thicknesses and Adhesive Strengths of Joints), Jpn Soc Mech Eng Int J, 1987; 30(265): 1042–51.

[18] Koguchi H, Muramoto T. The order of stress singularity near the vertex in three-dimensional joints, Int J Solids and Struct, 2000; 66(648): 1597–605.

[19] Bogy DB. Edge- Bonded Dissimilar Orthogonal Elastic Wedges under Normal and Shear Loading, Trans ASME, J Appl Mech, 1968; 35: 460–6.

[20] Bogy DB. Two Edge-Bonded Elastic Wedges of Different Materials and Wedge Angles under Surface Tractions, Trans ASME, J Appl Mech, 1971; 38: 377–86.

[21] Oda K, Takahata Y, Kasamura Y, Noda NA. Stress intensity factor solution for edge interface crack based on the crack tip stress without the crack, Eng Fract Mech, 2019; 219: 106612.

[22] Sawa T. -Passed with eyes- Practical skill test "Normal lathe work Grade 2" Procedure and explanation, Nikkankougyoushinbun, 2009 [in Japanese]

[23] Noda NA, Uchikoba T, Ueno M, Sano Y, Iida K, Wang Z, Wang G. Convenient debonding strength evaluation for spray coating based on intensity of singular stress, ISIJ International, 2015; 55(12): 2624–30.

[24] Wang Z, Noda NA, Ueno M, Sano Y. Optimum design of ceramic spray coating evaluated in terms of intensity of singular stress field, Steel Research Int, 2017; 88(7): 1600353.

[25] Takaki R, Noda NA, Sano Y, Takase Y, Suzuki Y, Chao CK, Chang K, Fracture Origin of Prismatic Butt Joints in Relation to the Intensity of Singular Stress Field (ISSF), Trans Jpn Inst Electron Packag, 2020; 23(6): 507–15.

[26] Timoshenko SP, Goodier JN, Theory of Elasticity Third Edition, McGraw-Hill, Inc. 1970.

[27] Agogino AM. Notch Effects, Stress State, and Ductility, Trans ASME, J Eng Mater & Tech, 1978; 100(4): 348–55.

[28] Adams RD, Coppendale BJ, The stress-strain behaviour of axially-loaded butt joints, J. Adhes, 1979; 10: 49–62.

[29] Ren F, Noda NA, Adhesive strength evaluation for three-dimensional butt joint in terms of the intensity of singular stress field on the interface outer edge, Int J Adhes Adhes, 2020, 98: 102549.

[30] Noda NA, Ren F, Takaki R, Wang Z, Oda K, Miyazaki T. Intensity of singular stress field over the

entire bond line thickness range useful for evaluating the adhesive strength for plate and cylinder butt joints, Int J Adhes Adhes, 2018; 85: 234–50.

[31] Miyazaki T, Noda NA, Ren F, Wang Z, Sano Y, Iida K, Analysis of intensity of singular stress field for bonded cylinder and bonded pipe in comparison with bonded plate, Int J Adhes Adhes, 2017; 77: 118–37.